Chinese Journal of Aeronautics, (2024), 37(7): 285–300

Chinese Society of Aeronautics and Astronautics
& Beihang University

Chinese Journal of Aeronautics

cja@buaa.edu.cn
www.sciencedirect.com


FULL LENGTH ARTICLE

# Design optimization and testing of a morphing leading-edge with a variable-thickness compliant skin and a closed-chain mechanism


**Zhigang WANG [a,b], Xiasheng SUN [c], Yu YANG [b], Wenjie GE [d], Daochun LI [a,*], Jinwu XIANG [a], Panpan BAO [b], Qi WU [b], Andrea DA RONCH [e]**

[a] *School of Aeronautical Science and Engineering, Beihang University, Beijing 100191, China*
[b] *National Key Laboratory of Strength and Structural Integrity, Aircraft Strength Research Institute of China, Xi'an 710065, China*
[c] *School of Aeronautics and Astronautics, Shanghai Jiao Tong University, Shanghai 200240, China*
[d] *School of Mechanical Engineering, Northwestern Polytechnical University, Xi'an 710072, China*
[e] *Faculty of Engineering and Physical Sciences, University of Southampton, Southampton SO17 1JB, UK*

Received 17 November 2023; revised 8 January 2024; accepted 20 March 2024
Available online 27 April 2024

**KEYWORDS**

Optimization;
Design;
Morphing wing;
Compliant skin;
Kinematics;
Leading-edge;
Control surfaces

**Abstract** Climate warming and the increased demand in air travels motivate the aviation industry to urgently produce technological innovations. One of the most promising innovations is based on the smoothly continuous morphing leading-edge concept. This study proposes a two-step process for the design of a morphing leading-edge, including the optimization of the outer variable-thickness composite compliant skin and the optimization of the inner kinematic mechanism. For the compliant skin design, an optimization of the variable thickness composite skin is proposed based on a laminate continuity model, with laminate continuity constraint and other manufacturing constraints. The laminate continuity model utilizes a guiding sequence and a ply-drop sequence to describe the overall stacking sequence of plies in different thickness regions of the complaint skin. For the inner kinematic mechanism design, a coupled four-bar linkage system is proposed and optimized to produce specific trajectories at the actuation points on the stringer hats of the compliant skin, which ensures that the compliant skin can be deflected into the aerodynamically optimal profile. Finally, a morphing leading-edge is manufactured and tested. Experimental results are compared with numerical predictions, confirming the feasibility of the morphing leading-edge concept and the overall proposed design approach.



* Corresponding author.
E-mail address: lidc@buaa.edu.cn (D. LI).

Peer review under responsibility of Editorial Committee of CJA.


https://doi.org/10.1016/j.cja.2024.04.021

## 1. Introduction

According to the WAYPOINT2050 of the Air Transport Action Group, in order to meet the requirements of the Paris Agreement on limiting global temperature rise, the aviation sector needs to realize zero carbon emissions by 2050 compared to 2005.[1] To achieve this goal, the aviation industry needs to develop a series of innovative technologies (such as advanced aerodynamic configurations, alternative energy sources, innovative structures, lightweight materials and efficient engines, etc.).[1] Some analysis shows that by 2050, these technological innovations can contribute up to 34% to the goal, and the morphing wing is one of the most important and promising technologies.[1,2]

Morphing leading-edges are one type of morphing wing structures which can deform seamlessly and smoothly according to the change of flight conditions. Studies have shown that such a morphing leading-edge offers advantages mainly in terms of cruising aerodynamic efficiency and noise reduction, which complies with the goal of emission reduction and green aviation well. Firstly, when a morphing leading-edge is used in conjunction with a morphing trailing-edge, it can improve the aerodynamic performance of the full envelope of a large transport aircraft, specifically in the cruising stage;[3,4] Secondly, due to its seamless and smooth structural surface, a wider laminar flow area can be obtained on the upper surface of a wing and a laminar flow flight can be better realized, which plays an important role in reducing drag.[4,5] In addition, studies have shown that 25% of the noise of traditional civil aircraft comes from wing structures during landing and takeoff, and its dominant part is caused by its discontinuous leading-edge.[4,6,7] However, a seamless and smooth morphing leading-edge can effectively avoid the problem.

In view of the above advantages, a large body of work exists on the design of morphing leading-edges, proposing a series of structural concepts, some of which are pretty close to practical engineering. For instance, in European project SARISTU,[8,9] a full-scale morphing wing prototype has been developed which is integrated with morphing leading and trailing edge featuring high technology-readiness-level. Furthermore, recently, in another European project CS2-AIRGREEN2,[10–16] a full–scale morphing droop nose prototype made of actual aeronautical materials has also been developed and tested for an advanced regional aircraft, which demonstrated the effectiveness of a compliant structure concept. Some detailed review of morphing leading-edges can be found in the literatures.[17–25] Analyzing these research, it can be found that the structural concepts of morphing leading-edges are basically realized with an internal kinematic mechanism and an external monolithic compliant skin in order to simultaneously meet high load-bearing and deforming capability for large civil aircraft case.[26–37] Herein, we refer to the rigid-compliant coupling structures. This form of structure can make good use of the large rotating and high load-bearing capacity of kinematic mechanisms and at the same time can realize a continuous and seamless aerodynamic surface.

For morphing leading-edge, the most important thing is the design of the outer compliant skin. With the high specific strength and stiffness, as well as the high ultimate strain and the capacity to tailor the mechanical behavior, composite materials especially variable-thickness glass-fiber reinforced laminate become the most effective solution for compliant skins. For variable-thickness compliant skin, the key problem is to determine the stacking sequences in different thickness regions of a compliant skin to ensure it can be precisely morphed into a target aerodynamic shape. Kintscher et al.[28,29] firstly proposed the concept of variable-thickness composite compliant skins in morphing wing design, and optimized the thickness distribution of a compliant skin through the Simplex method. On this basis, Vasista et al.[30] further considered the constraints of the maximum strain and local bending curvature of composite materials and a more sophisticated optimization model was developed using the same solving algorithm. With a similar structural scheme, Wang et al.[33] established theoretically the relationship between the target geometry and the bending stiffness distribution of a composite compliant skin, and determined its stacking sequence by an inverse method. For a morphing leading-edge with open-chain mechanism, Wang et al.[38–40] proposed a method to determine the stacking sequence of its composite material compliant skin. However, these methods do not consider ply continuity constraints in the design stage, which may lead to the fact that the obtained stacking sequences cannot be directly manufactured in practice, and some additional engineering adjustments are required. Regarding this problem, Rodenko et al. proposed an alternative design method with a Stacking Sequence Table (SST) to consider the laminate continuity constraint, but in the method a reasonable predefined lay-up table is needed.[29] When the maximum thickness of a variable-stiffness compliant skin is large, it is difficult to give out a reasonable SST manually. Therefore, it is necessary to establish an optimization method that can directly consider the laminate continuity constraint.

Another key problem for morphing leading-edge is the design of the internal kinematic mechanism. As for simplicity, most current morphing leading-edges are based on open-chain mechanisms whereby the internal rod linkage system is not a complete and independent mechanism if the outer compliant skin is removed. However, an open chain-mechanism has difficulty to maintain a specific aerodynamic shape particularly around areas of high negative or positive aerodynamic pressure. Further, the motion kinematics at some rod ends cannot be controlled, in turn causing a difficulty to control the aerodynamic profile of the compliant skin during the actuation of the morphing process. Nevertheless, if a closed-chain-based mechanism is applied, the outer surface profile will not be affected by the aerodynamic loads due to its independence because it has higher robustness for maintaining a specific aerodynamic shape. In general, a closed-chain internal mechanism is the preferred option.

The aim of this work is to propose a morphing leading-edge concept based on a variable-thickness compliant skin and a closed-chain-mechanism, and implements a two-step design approach for its design and optimization. In Section 2, the structural concept is discussed, as well as its aerodynamic shape and loads. In Section 3, the design method of the variable-thickness composite compliant skin is introduced. Section 4 focuses on the optimization method of the closed-chain mechanism, and Section 5 presents the results. Finally, conclusions are given in Section 6.

## 2. Design concept, geometry and loading

A CAE-GBJ (Chinese Aeronautical Establishment-Green Business Jet) developed by the Chinese Aeronautical Establish-

ment is utilized as the potential application airplane, and the anticipated overall layout of the morphing leading-edge in the aircraft is shown in Fig. 1. The aircraft is an intercontinental business jet with twin tail-mounted engines, a wingspan of 33.5 m and a length of 33 m. The cruise Mach number for this aircraft is 0.87.[41–43]

An actual wing is tapered and has a three-dimensional shape. As an initial verification of the design method, the real leading-edge is simplified into a two dimensional one using the same approach of Ref. 38. The initial shape of the leading-edge is selected from the in-line-of-flight wing cross-section extracted at a section of 30% from the fuselage, and its geometric dimensions are shown in Fig. 2. In order to reduce the strain level of the skin in drooped case, the constraint that the perimeter of the leading-edge profile remains constant is taken into account in the aerodynamic surface optimization of the target profile. It means there is only bending strain during drooping process, but no tensile strain, which is beneficial to improve the morphing capacity of the leading-edge. The design philosophy is defined as a "pure bending" principle herein. Regarding the aerodynamic design of the morphing leading edge, the initial aerodynamic profile is determined by Hua et al., specifically in Refs. 42, 43, and has been verified by a CAE-AVM wind tunnel test. The basic profile for the wing is NPU-SP6 with a 13% thick supercritical airfoil with a designed cruise speed of Mach 0.85. Furthermore, the target profile of the morphing leading edge is obtained through CFD analysis and optimization with the design objective of maximizing the lift coefficient at Mach 0.2 and 14° angle of attack in take-off case. The final optimized profile possesses a deflection angle of 20° and a leading edge radius of 16 mm. Detailed aerodynamic optimization is not the subject of this paper and can be found in the literature.[42] Fig. 3 shows the aerodynamic pressure distribution of the airfoil section in drooped case. The skin of the leading-edge needs to bear a large aerodynamic load during takeoff and landing, and it should be accounted in design phase. Therefore, the skin needs to have high deformability and high load-bearing capacity.

Due to the higher robustness of maintaining a specific aerodynamic profile, a rigid-compliant coupling structure based on the concept of closed-chain mechanism is adopted in the morphing leading-edge design. As shown in Fig. 4, the design of the morphing leading-edge can be further split into two phases: the design of the outer variable-stiffness compliant skin and the inner closed-chain actuating mechanism. For the design of the complaint skin, the key problem is to determine the stiffness distribution of the compliant skin; while for the inner mechanism, it is to synthesize the specific topology and shape of the mechanism.

To improve structural efficiency and deviation precision, a laminate with variable thickness or variable stiffness along the circumferential direction is a preferred option for the complaint skin, and the specific laminate sequence should be determined through an optimization design. Due to the strong designability and high ultimate strain, an aerospace-grade glass fiber composite was used here. This paper specifically adopted a woven glass fiber reinforced prepreg of SW100A/6511 with epoxy resin matrix manufactured by Guangwei Composite Materials Company, and the mechanical properties of the unidirectional laminate, which have been determined through material performance tests, are shown in Table 1. Herein, $E_1$ and $E_2$ are the elastic modulus of the prepreg parallel and perpendicular to the fiber directions; $Nu_{12}$ is the Poisson's ratio of the prepreg; $G_{12}$ is the shear modulus of the prepreg; $\varepsilon_t$ and $\varepsilon_c$ are the tensile and compressive ultimate strain of the prepreg respectively.

## 3. Design of variable-thickness composite compliant skin

### *3.1. Ply continuity model of variable-thickness compliant skin based on ply-drop sequence*

To complete the complex optimization problem, first it is necessary to have a simple and effective method to describe or define the stacking sequences of a variable-thickness composite compliant skin. Moreover, the method should have the ability to produce a laminate naturally meeting ply continuity and other criteria demanded by manufacturing process.

#### *3.1.1. Ply continuity criterion*

The ply continuity criterion requires that at every interface between two adjacent thickness regions the plies of the respective thinner region should cover the complete rest of the structure, the purpose of which is to improve the manufacturability of multi-region laminated structures and ensure structural integrity in the entire structure.[44] For example, suppose there are two adjacent laminates A and B, and A is thicker than B; if the ply stacking sequence of A is a "subset" of that of B, i.e. all ply angles of B originate from those of A, and the relative positions of the ply angles in B in the thickness direction should be consistent with those in A, then A and B satisfy the ply continuity criterion.

To better explain the ply continuity, a cross-section of a laminated structure is shown in Fig. 5. In the structure, there

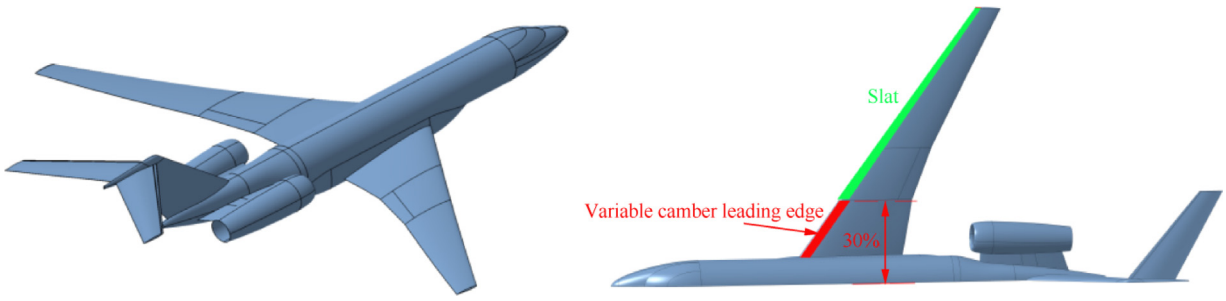


**Fig. 1** Model of green business jet and layout of high-lift device proposed by Chinese Aeronautical Establishment (CAE).

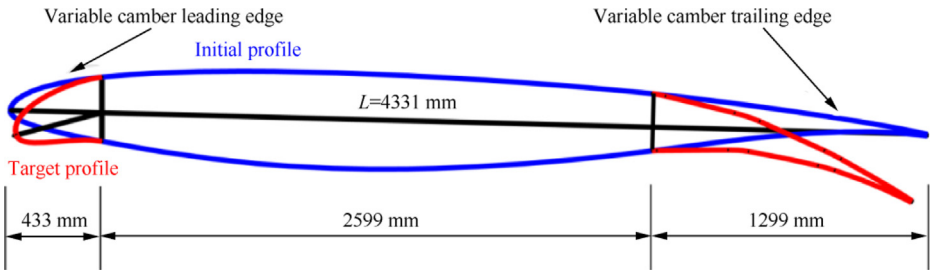


**Fig. 2** Airfoil profiles at design section before and after drooping.

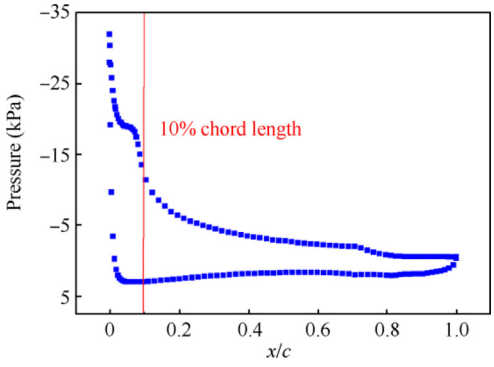


**Fig. 3** Pressure distribution of airfoil with morphing leading- and trailing-edge in drooped case.

is perfect continuity between laminates I and II, since their ply stacking sequences are the same. However, there is a thickness change between laminates II and III. Compared with laminate II, there is a ply-drop in laminate III, and on the contrary, laminate II implements ply addition operation relative to laminate III. The ply stacking sequence (3,1) of laminate III is a "subset" of the sequence (3,2,1) of laminate II. And all other single layers remain continuous between the two laminates, so the two laminates satisfy ply continuity. In addition, the thickness change is located between two consecutive plies, and there are other plies covering the ply-drop or added ply, which can effectively reduce the risk of delamination. As for the final laminate IV, due to the adoption of a new single layer marked in red, it does not meet the definition of "subset" between laminates II and III. Specifically, there is an angle conflict at the splice between ply-1 and the newly added ply-4, which will lead to stress concentration near this position. Laminates III and IV do not meet the ply continuity criterion.

### *3.1.2. Ply continuity model based on concept of guiding sequence and ply-drop sequence*

As illustrated above, if there is not any constraint for two adjacent stacking sequences, they may not meet the ply continuity criterion. Here, a ply continuity model is introduced to tackle this problem based on the concept of guiding sequence and Ply-Drop Sequence (PDS). With the model, the process of building the stacking sequence of a variable-thickness laminated structure is described below. As shown in Fig. 6, the structure consists of three regions or panels, denoted by Region 1, Region 2, and Region 3. Assuming that the thicknesses of the three panels are 2 plies, 4 plies and 3 plies, respectively, and the corresponding guiding sequence is (30 45 0 30 −45 90), and a positive integer sequence (1 2 3 4 5 6) is used, respectively, to indicate the positions of the six single plies in the thickness direction (from top to bottom). For instance, as for Region 2, their ply angles correspond to 4 certain single plies in the guiding sequence, which means that two single plies should be deleted from the guiding sequence with a thickness of 6 plies. Using the drop-off rules defined by the ply-drop sequence, it is possible to determine which individual plies are to be dropped off from the guiding sequence. Assuming that the ply-drop sequence is (2 4 3 6 1 5), the positions of the two single plies to be deleted in the guide are ply-2 and ply-4 respectively, and the corresponding ply angles are −45° and 30° respectively. After removing these two layers, the

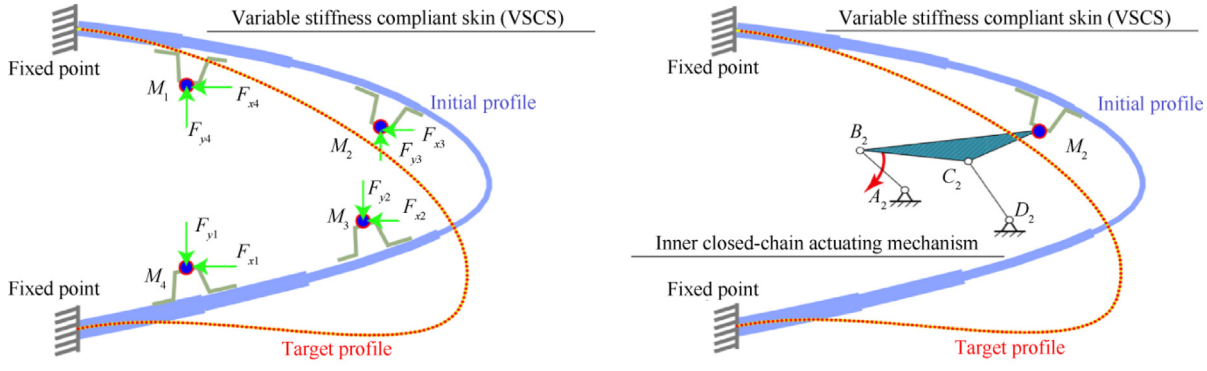


**Fig. 4** Morphing leading-edge based on concept of rigid-compliant coupling structures.

**Table 1** Mechanical properties of glass fiber reinforced prepreg.

| $E_1$ (GPa) | $E_2$ (GPa) | $Nu_{12}$ | $G_{12}$ (GPa) | $\varepsilon_t$ (με) | $\varepsilon_c$ (με) |
|---|---|---|---|---|---|
| 47.7 | 13.3 | 0.12 | 47.5 | 33166 | 13538 |

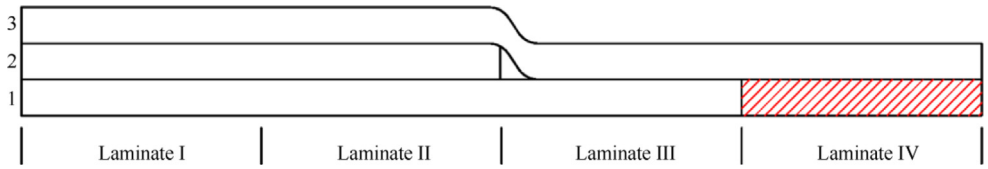


**Fig. 5** Schematic diagram of ply continuity criterion.

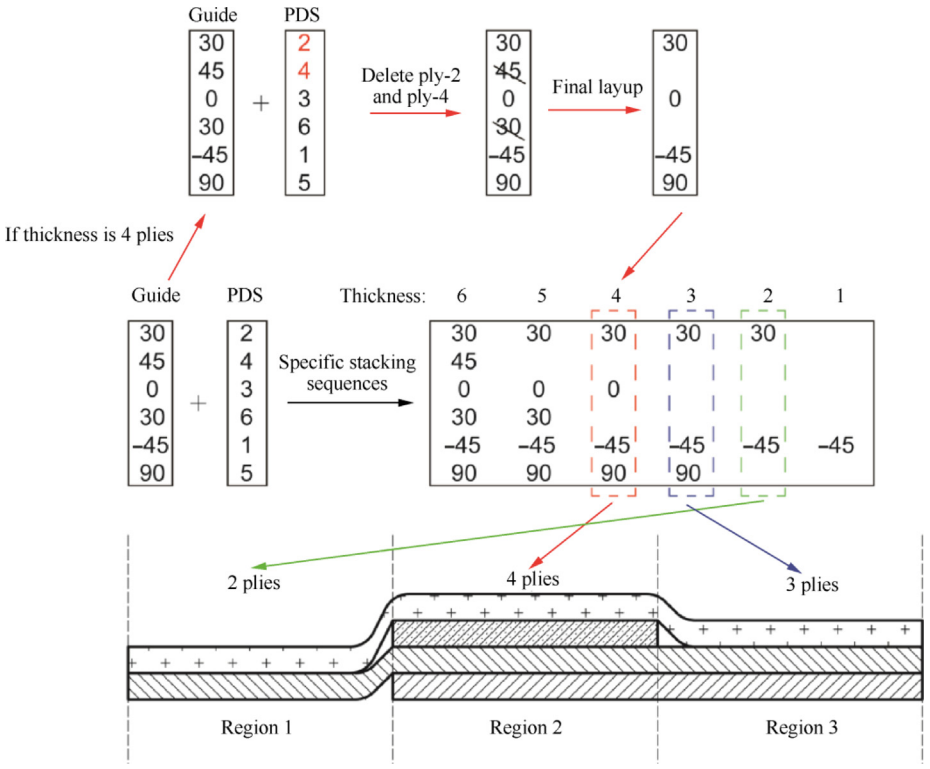


**Fig. 6** Schematic diagram of fiber continuity model based on a ply-drop sequence.

remaining stacking sequence is (30 0 −45 90), which is also the ply structure for Region 2. In the same way, after deleting ply-3 and ply-6 (0° and 90° plies) in turn, the stacking sequences of Region 3 and Region 1 are (30 −45 90) and (30 −45) respectively.

It can be found from the figure that the process of building laminates through the ply-drop sequence is very simple, as it just needs to "read" the corresponding ply from the guiding sequence according to the specific ply thickness, instead of relying on a complex Stacking Sequence Table (SST). From the above diagram, it can also be seen that the drop-off plies in the thickness direction is completely achievable in engineering as the multi-region laminated structure described by the model satisfies the ply continuity criterion well. In addition, it should be noted that the ply-drop sequence is only used to specify drop-off rules, not to change the guiding sequence, and it only works when the thickness of the laminate changes. In other words, if an area has the same thickness as the guide, the stacking sequence for the laminate will always be the same as the guide, regardless of the drop-off rule specified by the ply-drop sequence.

In addition to the ply continuity criterion, the following criteria often should be considered for each region of a variable-thickness compliant skin according to the composite material design guide:[44] (A) in order to simplify design, analysis and manufacturing process, a fixed angle increment should be adopted; (B) layups should be arranged symmetrically along thickness direction; (C) it is necessary to avoid using ply

groups in the same ply angle, and if used, no more than 4 consecutive layers; (D) the outermost layer of a layer-up cannot be dropped-off to avoid delamination.

### 3.2. Optimization of variable-thickness compliant skin

In addition to the distribution of skin stiffness, the position of the stringers and the magnitude of the transmitted loads on the stringer hats also have a great influence on the final drooped shape. Therefore, the variables that need to be determined in the compliant skin design include the stacking sequence of each region, the position of each stringer, and the transmitted load of each stringer, which is a typical multi-class-variable optimization problem (contains discrete and continuous variables simultaneously) as shown in Fig. 7. Compared with gradient algorithms, Genetic Algorithms (GA) are more prominent in discrete variable optimization problem, so they are also more suitable for solving this problem.

#### 3.2.1. Mathematic model of optimization

Using the structural concept, this paper firstly establishes the finite element model of the compliant skin. As mentioned before, as an initial verification case, the morphing leading-edge is simplified as a two-dimensional structure with a span-wise length of 350 mm, and there is only one set of inner kinematic mechanism in span direction deployed to drive the compliant skin to the target shape.

As shown in Fig. 8, in its finite element model, a fixed boundary condition is applied to the upper and lower ends of the compliant skin as they should be connected to a fixed front spar in real environment. According to the analysis in Section 2, the inner kinematic mechanism transmits the actuator force to the compliant skin through the four hinge points on the stringer hats, so a load boundary condition is used here to simulate the transmitted forces. Each transmitted force includes both horizontal and vertical components. Since the magnitude of the transmitted forces is related to the stiffness distribution of the skin and the stringer positions, these components are unknown variables that need to be optimized during the optimization process, and there are 8 components in total. Besides the four concentrated forces, a distributed aerodynamic pressure is also exacted on the outer surface of the complaint skin according to the flight condition in take-off case. Moreover, in the finite element model, 14600 linear quadrilateral shell elements are used to simulate the compliant skin with an element size of 4.5 mm and all stringers are also simulated by the same element type with a constant ply numbers of 15. To simulate the connecting interaction between the stringers and the compliant skin, a type of TIE connector elements, defined by Abaqus software, is utilized with a default position tolerance.

Another problem in variable-thickness compliant skin design is the determination of the number of skin partitions. In fact, to obtain the best skin stiffness distribution, the thickness partitions of the skin should be as many as possible; but more skin partitions will reduce the manufacturability of the skin, such as the minimum allowable size of the skin partition and the restrictions on the size of the layer stacking equipment. Therefore, considering the above constraints, this paper divides the compliant skin into 10 thickness regions along the circumferential direction. According to the relationship between curvature and thickness, the maximum thickness is determined to be 36 layers; due to the consideration of the symmetrical ply constraints, the actual guiding layer sequence is 18 layers. According to the ply continuity model based on the ply-drop sequence in Section 3, the design variables to describe the ply distribution of the compliant skin include: 18 angle values for the guiding sequence, 18 integer values for the ply-drop sequence and 10 thickness values for the thickness distribution. To sum up, after adding the eight force component variables in the four stringers, the total number of design variables is 58.

Compared with the current compliant skin design methods in the literatures,[27,28,45,46] this paper comprehensively considers the skin weight, deformation accuracy, non-balance constraint and violation of the maximum number of consecutive identical plies in the optimization design objectives. To unify these four factors into one single objective function, this paper proposes the following objective function (or fitness function) to address the problem. Moreover, to effectively evaluate these constraints, the deviation, non-balance constraint and consecutive ply number are normalized as shown:

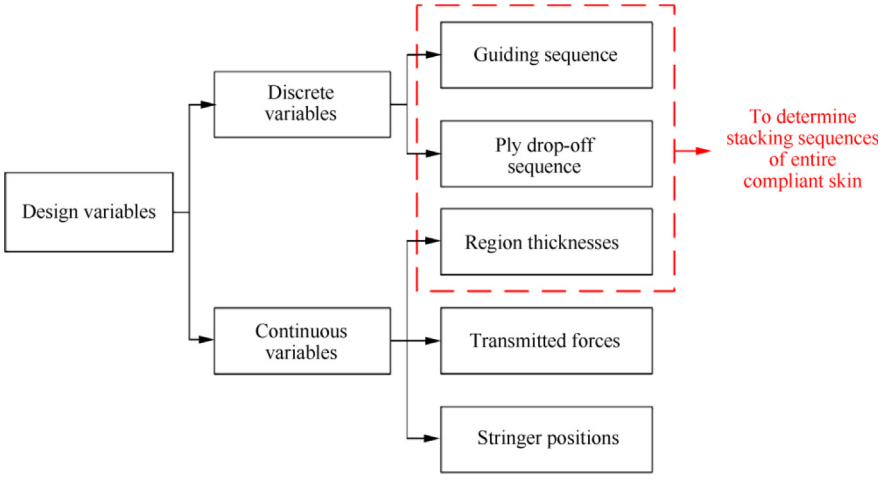


**Fig. 7** Discrete and continuous variables of compliant skin design problem.

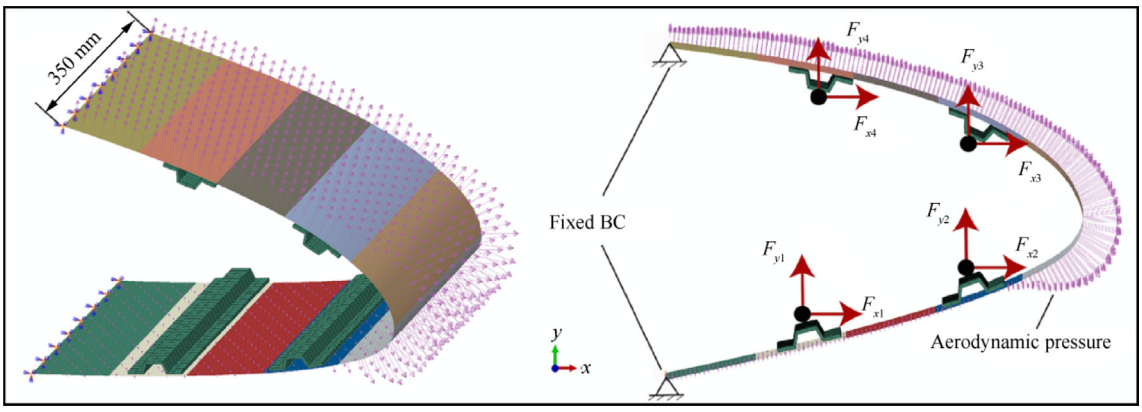


**Fig. 8** Finite element model of compliant skin.

$$\text{fitness}(s_n, g_i, d_j, t_k) = \begin{cases} V_{\text{CompliantSkin}} \times (1 + \alpha \times C_{\text{crit\_con}}), & \text{if } C_{\text{crit\_con}} \leqslant 0 \\ V_{\text{CompliantSkin}} \times (1 + 0.1 + \beta \times C_{\text{crit\_con}}), & \text{if } C_{\text{crit\_con}} > 0 \end{cases} \tag{1}$$

$$C_{\text{crit\_con}} = \text{maximum}\left(1 - \frac{1}{D_{\text{deviation}}}, \frac{\text{NB}_{\text{sum\_nonbalance}}}{\text{MaxLayerNumber}}, C_{\text{count\_succ}}\right) \tag{2}$$

where $D_{\text{deviation}}$ is the deviation between the target shape curve and the achieved shape curve, which is described by the Least Square Error (LSE) of the coordinates of overall control points on these two curves; $V_{\text{CompliantSkin}}$ is the laminate volume of the entire complaint skin to evaluate its mass indirectively; $C_{\text{crit\_con}}$ is the critical values to evaluate the deviation, non-balance constraint and the violation of the maximum number of consecutive identical plies; $\text{NB}_{\text{sum\_nonbalance}}$ is the sum of the non-balance layers; $C_{\text{count\_succ}}$ is the number of the successive identical plies; $\alpha$ and $\beta$ are the corresponding weight factors in different constraint conditions.

Therefore, the final mathematical optimization model is established as follows:

$$\begin{cases} \min & \text{fitness}(g_i, d_j, t_k, f_m, s_n) \\ \text{s.}t. & K(U)U = F(U) \\ & g_i \in [\pm 75^\circ, \pm 45^\circ, \pm 30^\circ, \pm 15^\circ, 0^\circ, 90^\circ], i = 1, 2, ..., \text{MaxLayerNumber} \\ & d_j \in [1, 2, ..., \text{MaxLayerNumber}], j = 1, 2, ..., \text{MaxLayerNumber} \\ & t_k \in [1, \text{MaxLayerNumber}], k = 1, 2, ..., \text{RegionNum} \\ & f_m \in [\text{Lower}, \text{Upper}], m = 1, 2, ..., 8 \\ & s_n \in (0, 1), n = 1, 2, 3, 4 \end{cases} \tag{3}$$

where $\text{fitness}(g_i, d_j, t_k, f_m, s_n)$ is the objective function; $K(U)U = F(U)$ is the equilibrium equation of the overall finite element model; MaxLayNumber is the maximum permitted half layer number of the variable-thickness compliant skin determined by the relationship between the maximum curvature change and corresponding thickness according to Euler beam theory. Here, we are going to take 16; RegionNum is the thickness region number of the compliant skin, which is taken as 10 here empirically to balance the morphing accuracy and the manufacturing complexity; Lower and Upper are the lower and upper boundaries of the transmitted forces respectively determined by several tentative calculations to ensure that they can produce a drooping angle far large than one of the target profile; $g_i$ is the $i$th variable in the guiding sequence; $d_j$ is the $j$th variable in the ply-drop sequence; $t_k$ is $k$th region's thickness; $f_m$ is the $m$th component of the transmitted forces; $s_n$ is the $n$th stringer's position.

### 3.2.2. Optimization results

Finally, the optimization problem is solved by a GA solver and the iteration process is shown in Fig. 9. It can be seen that the objective function ultimately converges to $3.11 \times 10^7$ after 268 iterations. According to the definition of the objective function in last section, it is a synthesized value which simultaneously reflects the structural volume (or weight), the final deviation, the non-balance constraint, and the violation of the maximum number of consecutive identical layers. Fig. 10 presents the iterative results of each single factor. Fig. 10(a) shows the iteration process of the structural volume and the volume value first decreases and then increases to obtain a smaller comprehensive objective function value. And it can be seen from Fig. 10(b) that the final deviation or LSE value converges to 1.02 mm, which indicates that the mean deviation value is 1.02 mm. Fig. 10(c) shows that the ratio of the non-balance layer number to the maximum layer number converges from 11 to 0 almost. Fig. 10(d) shows that there is not any consecutive layer in which the layer number is more than four in all stacking sequences of the final optimal compliant skin.

After reconstructing the finite element model according to the optimal design variable values, the finite element analysis model of the optimal compliant skin can be obtained as shown in Fig. 11. The maximum tensile strain of the compliant skin at

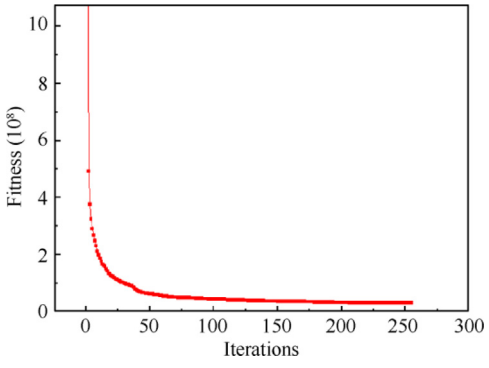


**Fig. 9** Iterative process of objective function (or fitness function).

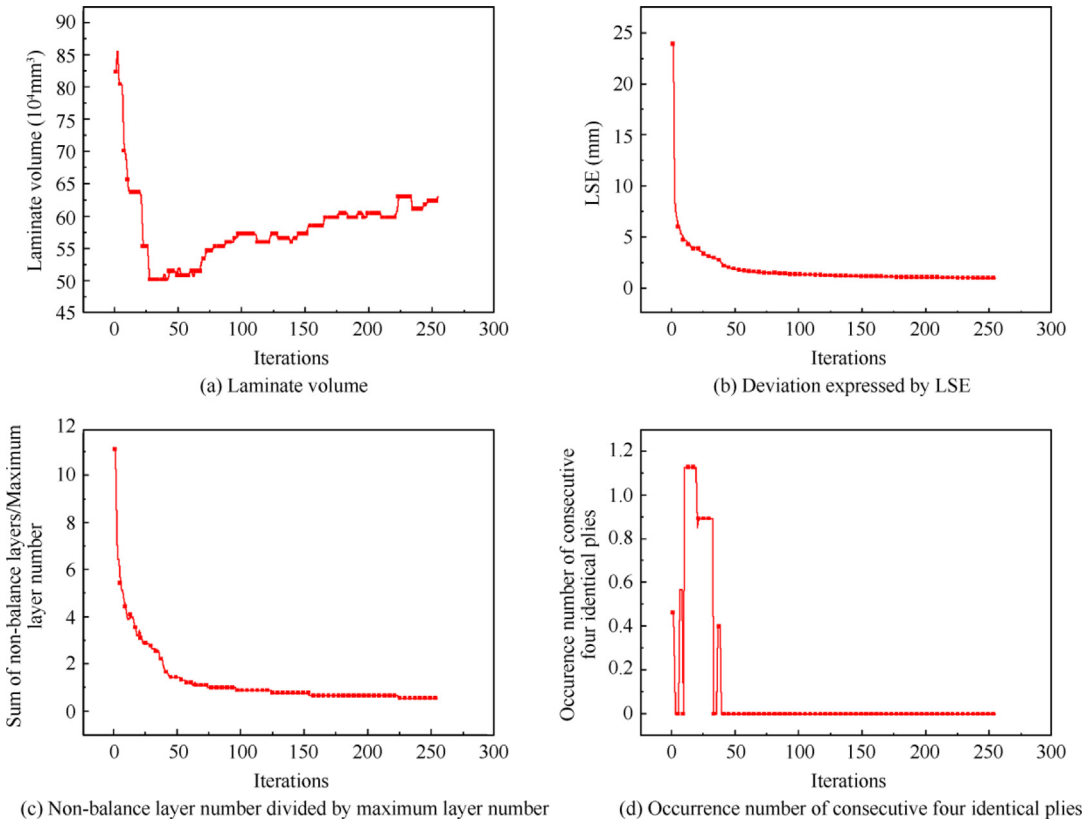


**Fig. 10** Iteration process of every individual factor.

drooped state is 11830 με, which is less than the tensile limit of the composite material and meets the requirements of structural strength.

The deformed shape is extracted and compared with the target shape as shown in Fig. 12(a). It is found that the final shape is in good agreement with the target shape, and the maximum deviation is located at the middle point of the lower surface. In addition, analyzing the distribution of the deviation along the circumferential direction as shown in Fig. 12(b), one finds that the largest deformation errors are mainly distributed at 20% and 50% of the complaint skin with deviation values of 3.6 mm and 3.3 mm respectively. This phenomenon can be explained by analyzing the curvature change between the target profile and the initial profile. It is mainly due to the large curvature variations at these points, which makes it difficult to precisely control every point on the complaint skin just through four stringers.

Finally, Fig. 13 presents the optimal stacking sequence distribution corresponding to each region of the compliant skin. It can be seen that to resist aerodynamic loads, the thinnest plies of the flexible skin should be greater than 20 plies. In the optimization process, to ensure a continuous most-outer layup in different regions, a 90° prepreg layer is always arranged on the upper and lower surfaces of the compliant skin. The final maximum thickness of plies is 32, which was less than the upper limit of the thickness design variable. In addition, it can be seen from the stacking table that the expected ply continuity requirements are achieved between all partitions, which is beneficial to avoiding stress concentration; there are no consecutive four layers with the same angle in the table, which meets the constraint of no more than four consecutive identical layers. It can also be seen that all stacking sequences meet the balance constraint. Therefore, the result of the stacking sequences verifies the effectiveness of the above ply continuity model in the optimal design of the compliant skin.

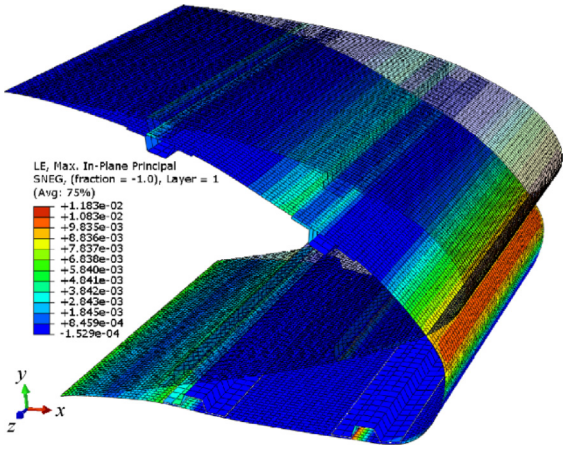


**Fig. 11** Optimized initial shape and deformed shape of compliant skin and its strain distribution.

## 4. Design of closed-chain kinematic mechanism

### *4.1. Synthesis of coupling four-bar linkages system*

The solution of the compliant skin optimization can determine the optimal positions of the four stringers and ply stacking

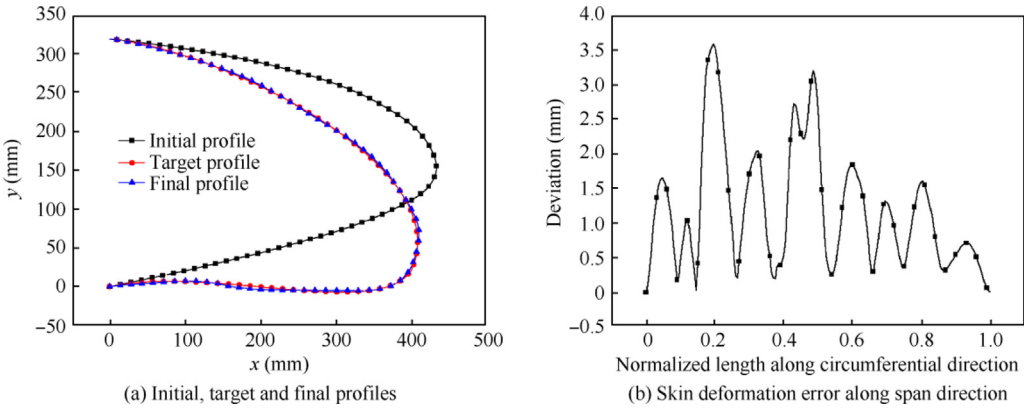


(a) Initial, target and final profiles (b) Skin deformation error along span direction

**Fig. 12** Comparison of initial, target and final profiles and deformation error distribution.

| Inner surface of compliant skin | | | | | | | | | | |
|---|---|---|---|---|---|---|---|---|---|---|
| | Region 1 | Region 2 | Region 3 | Region 4 | Region 5 | Region 6 | Region 7 | Region 8 | Region 9 | Region 10 |
| ply-1 | 90° | 90° | 90° | 90° | 90° | 90° | 90° | 90° | 90° | 90° |
| ply-2 | | | −15° | −15° | | | −15° | −15° | −15° | −15° |
| ply-3 | −75° | −75° | −75° | −75° | −75° | −75° | −75° | −75° | −75° | −75° |
| ply-4 | | | | | | | | 90° | | |
| ply-5 | 15° | 15° | 15° | 15° | 15° | 15° | 15° | 15° | 15° | 15° |
| ply-6 | | 30° | 30° | 30° | 30° | 30° | 30° | 30° | 30° | 30° |
| ply-7 | | | | 90° | | | 90° | 90° | 90° | |
| ply-8 | | | | | | | | 90° | 90° | |
| ply-9 | | | 0° | 0° | | | 0° | 0° | 0° | |
| ply-10 | | −30° | −30° | −30° | −30° | −30° | −30° | −30° | −30° | −30° |
| ply-11 | | | | | | | | 30° | | |
| ply-12 | | | 0° | 0° | | | 0° | 0° | 0° | 0° |
| ply-13 | | | | | | | 15° | 15° | 15° | |
| ply-14 | −15° | −15° | −15° | −15° | −15° | −15° | −15° | −15° | −15° | −15° |
| ply-15 | | | 90° | 90° | 90° | 90° | 90° | 90° | 90° | 90° |
| ply-16 | 75° | 75° | 75° | 75° | 75° | 75° | 75° | 75° | 75° | 75° |
| Symmetry plane | | | | | | | | | | |

**Fig. 13** Ply stacking sequences of different regions of optimal compliant skin.

sequences of the compliant skin. Through executing non-linear finite element calculation, it can further give out the corresponding movement trajectories of the actuated points on the stringer hats in the drooping process as shown in blue in Fig. 14. Therefore, these target trajectories are utilized as the design objective for the internal kinematic mechanism design and the task is to synthesize one set of internal kinematic mechanism which can produce these trajectories at the actuated points. As shown in Fig. 14, $M_1$ to $M_4$ represent the initial positions of the four actuated points and $M_1'$–$M_4'$ represent the final positions of them respectively. The four blue lines are the corresponding movement trajectories.

From the view of decreasing complexity, a Watt six-bar mechanism[47] is an ideal closed-chain actuating kinematic mechanism. However, it is difficult to ensure that all the produced movement trajectories can agree well with the optimal trajectories. Moreover, it can be seen that all the target trajectories are not complex, which means the simplest closed-chain four-bar linkage can achieve a good match. As one set of four-bar linkage can ensure only one target trajectory, four sets of them are needed and there are four control degrees of freedom

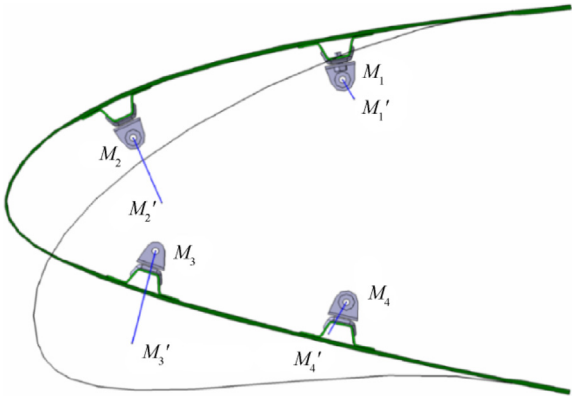


**Fig. 14** Optimal movement trajectories of actuated points.

which would increase the complexity. Therefore, a coupling four-bar linkage system concept is proposed to ensure that only one actuator is needed to actuate four sets of four-bar linkage simultaneously.

The coupling method of four-bar linkages is shown in Fig. 15(a). In the linkage system, there are four sets of four-

bar linkages represented as $A_i - B_i - C_i - D_i (i = 1, 2, 3, 4)$, and $M_i (i = 1, 2, 3, 4)$ are the four actuated points(or control points) on the stringers respectively. Every control point is connected with $B_i - C_i$ fixedly. $E_i (i = 1, 2, 3)$ represents the three coupling points and each of them are fixed with one bar and hinged with one another bar.

Inversion method[48] is applied to determine the specific coordinates of coupling points, as shown in Fig. 15(b). When two adjacent four-bar linkages are determined, their motion processes or laws are also determined. Assume that $A_1 - B_1, A_1 - B_1', A_1 - B_1''$, and $A_2 - B_2, A_2 - B_2', A_2 - B_2''$ are three motion states of these two adjacent four-bar linkages correspondingly. And they associate to initial, intermediate and final states respectively. In inversion method, $A_1 B_1' B_2'$ and $A_1 B_1'' B_2''$ are seen as rigid body and rotated by $\theta_1$ and $\theta_2$ about fixed point $A_1$. The point $B_2'$ and point $B_2''$ are moved to $B_{2x}'$ and $B_{2x}''$ respectively. According to the inversion principle,[48] coupling point $E$ must locate at the intersection point of the mid-perpendicular lines of $B_2 B_{2x}'$ and $B_{2x}' B_{2x}''$. Similarly, the other two coupling points can be determined with the same method.

### 4.2. Optimization of linkages system

#### 4.2.1. Optimization model

With the coupling method, the other core problem is the synthesis of the four sets of four-bar linkage. To ensure every control point to produce predefined trajectory precisely, it is necessary to optimize every single four-bar linkage.

Fig. 16 is the diagram of the fourth set of four-bar linkage and the produced and target trajectories of the four control points. For the fourth linkage, point $A$ and point $D$ are the fixed points. $AB$, $BC$ and $CD$ denote rod-1, rod-2 and rod-3 respectively. $\theta_1, \theta_2, \theta_3$ and $\theta_4$ associate to the angles between the four rods and abscissa axis. $M_4$ represents the fourth control point and $BCM_4$ is a rigid panel. $(x_{M1'}, y_{M1'})$ and $(x_{M2'}, y_{M2'})$ denote the middle and final points of the $M_4$ along the target trajectory, while $(x_{m1'}, y_{m1'})$ and $(x_{m2'}, y_{m2'})$ along the produced(or actual) trajectory.

Assume the length of rod-1, rod-2, and rod-3 is represented as $l_1$, $l_2$ and $l_3$. Through vector calculation, the coordinates of the points $B$ and point $C$ can be expressed as

$$\begin{bmatrix} x_B & x_C \\ y_B & y_C \end{bmatrix} = \begin{bmatrix} x_A + l_1 \cos\theta_1 & x_D + l_3 \cos\theta_3 \\ y_A + l_1 \sin\theta_1 & y_D + l_3 \sin\theta_3 \end{bmatrix} \tag{4}$$

where $(x_B, y_B)$, $(x_C, y_C)$ and $(x_D, y_D)$ represent the coordinates of the point $B$, $C$ and $D$.

Additionally, through a closed-loop vector calculation, there is a geometrical relationship within the four-bar linkage given as

$$\begin{bmatrix} l_1\cos\theta_1 + l_2\cos\theta_2 \\ l_1\sin\theta_1 + l_2\sin\theta_2 \end{bmatrix} = \begin{bmatrix} l_3\cos\theta_3 + l_4\cos\theta_4 \\ l_3\sin\theta_3 + l_4\sin\theta_4 \end{bmatrix} \tag{5}$$

where $\theta_4 = \arctan\frac{y_A - y_D}{x_A - x_D}$.

As the initial coordinate of the point $M_4$ is predefined, the length of $BM_4$ and $\beta$ can be obtained easily by triangular calculation. And its final coordinate can be expressed as

$$\begin{bmatrix} m_x \\ m_y \end{bmatrix} = \begin{bmatrix} x_B + d\cos(\theta_2 + \beta) \\ y_B + d\sin(\theta_2 + \beta) \end{bmatrix} \tag{6}$$

where $(m_x, m_y)$ is the coordinate of the point $M_4$ and $d$ is the length of $BM_4$.

As illustrated previously, the design objective of the kinematic mechanism is to synthesize a mechanism which can produce motion trajectories as close as possible to the target trajectories of the four control points. Therefore, for the fourth linkage, the objective function and optimization model can be expressed as

$$\begin{cases} \min F(l_1, l_2, l_3, \theta_1, \Delta\theta_1, \Delta\theta_2, x_A, y_A, x_D, y_D) = \sum_{i=1}^{2} \left[ (x_{mi'} - x_{Mi'})^2 + (y_{mi'} - y_{Mi'})^2 \right] \\ s.t. \quad l_i \in (30, 250), i = 1, 2, 3 \\ \theta_1 \in [-\frac{\pi}{3}, \pi]; \Delta\theta_1 \in [-\frac{\pi}{6}, \frac{\pi}{6}]; \Delta\theta_2 \in [-\frac{\pi}{6}, \frac{\pi}{6}] \\ x_A \in [20, 200]; y_A \in [20, 200] \\ x_D \in [20, 200]; y_D \in [20, 200] \end{cases} \tag{7}$$

where $\theta_1$ is the angle of the rod $AB$ in initial case; $\Delta\theta_1$ and $\Delta\theta_2$ represent the angle increment of the rod $AB$ in the two actuated states; $(x_A, y_A)$ and $(x_D, y_D)$ are the coordinates of the point $A$ and point $D$; $l_i$ is the length of the $i$th rod.

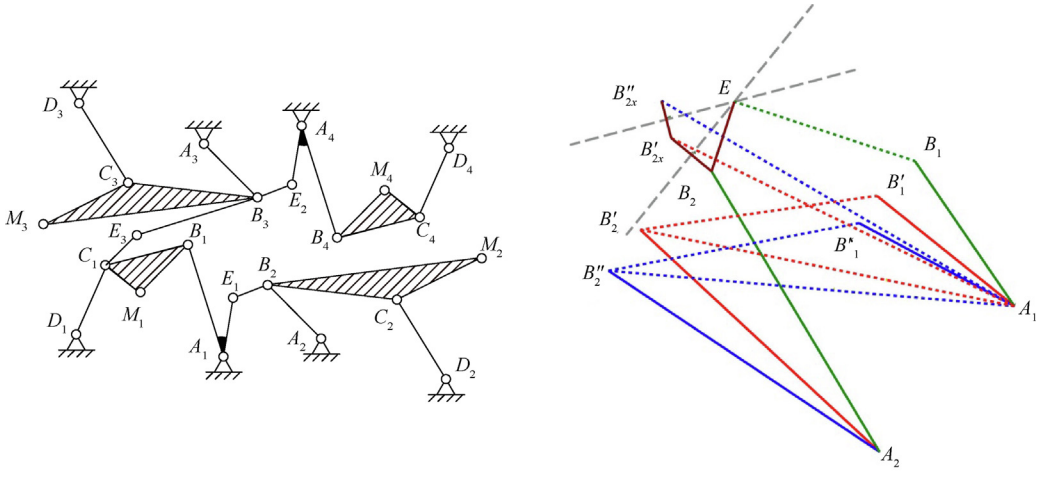


(a) A coupling four-bar linkage system (b) Diagram of determining coordinates of coupling point

**Fig. 15** Coupling method of four-bar linkages.

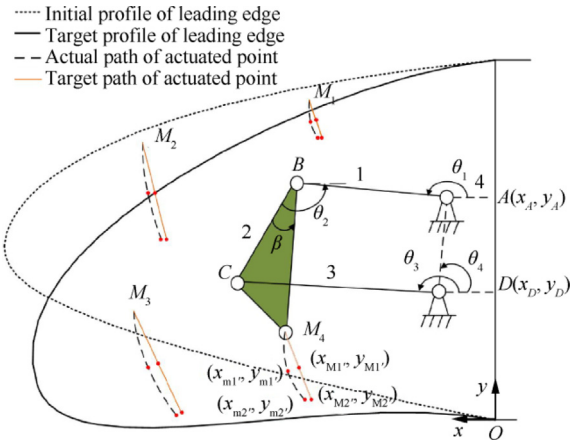


**Fig. 16** Diagram of one set of four-bar linkage and actual and target trajectories of four control points.

After the establishment of the optimization model, there are three principles for the determination of the lower and upper boundaries of all the design variables. Firstly, all the kinematic mechanism should always within the inner space encircled by the outer compliant skin and the front spar; secondly, some margins from the compliant skin should be maintained to ensure enough operation space for installation. In addition, all the rods should be arranged as close as to the compliant skin to avoid a set of heavy linkage system with a large continuous volume of the rods. Finally, the optimization problem is solved with a genetic algorithm. Similarly, the other three sets of individual optimization problems can be formulated and solved.

### 4.2.2. Optimization results

Fig. 17 is the mechanism configurations of the final optimal four sets of the four-bar linkage before and after drooping. It can be seen that all the four sets of linkage are encircled in the compliant skin. In order to analyze the deviation between the actual trajectories and the target trajectories, these trajectories are presented in the Fig. 18. It can be seen that the actual trajectories of the control points $M_1$, $M_2$ and $M_4$ agree well with their target trajectories, while the trajectory deviation of the control point $M_3$ is a little large.

With the optimized internal kinematic mechanism and the outer compliant skin, a multi-body dynamic model was established to analyze the final morphing profile and the material strain distribution. Fig. 19 shows the multi-body dynamic model of the morphing leading-edge and the calculated strain distribution result. During the concept design phase, all linkages are modeled with ideal rigid elements to spare calculation cost, but it will be analyzed further with real elastic elements in the detailed design phase as shown in the following section. In the multi-body dynamic model, the distributed aerodynamic pressure on the compliant skin is also included. From the strain contour, the maximum strain of all the layers of the composite complaint skin is around 9937 με which is less than

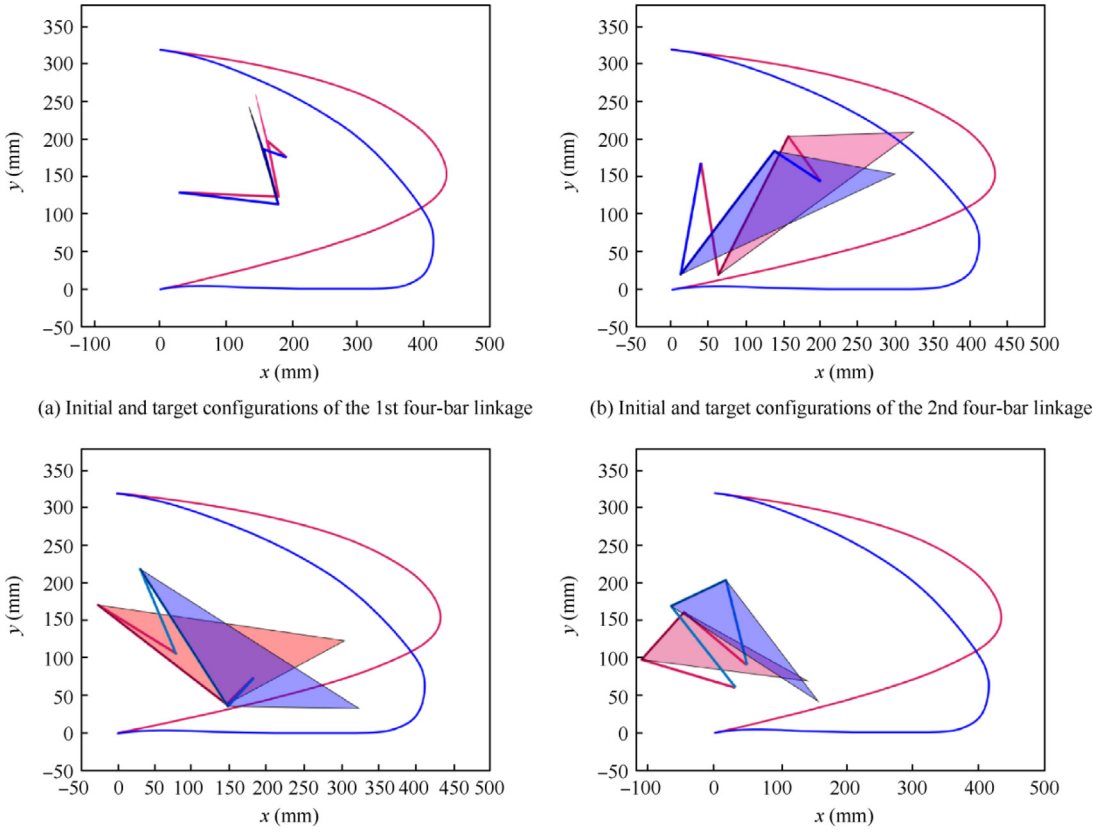


**Fig. 17** Initial and target configurations of optimal four sets of four-bar linkage.

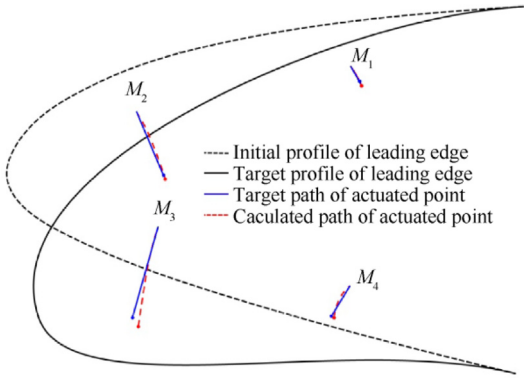


**Fig. 18** Comparison between actual and target trajectories of four control points.

the ultimate strain of the selected material. Furthermore, it can be seen that the large strain region distributes around the most leading end. Fig. 20 shows the comparison between the target and the calculated profile and its deviation distribution along the circumferential direction of the compliant skin. It can be seen that the two profiles agree well in general and the maximum deviation is about 7.43 mm located at around 0.3 from the bottom end of the skin.

## 5. Physical mock-up, testing and results

With the design results of the outer compliant skin and the inner kinematic mechanism, a physical mock-up of the morphing leading-edge was developed as shown in Fig. 21. For the mock-up, all linkages were dimensioned with titanium alloy Ti-6Al-4V with yield strength of 880 MPa to ensure its stiffness and decrease weight. With limited installation space, a brass worm gear and an electrical motor were utilized to driven the linkage mechanism. To estimate the strength of every individual linkage part before fabrication, a multi-body dynamic analysis model was established to examine its stress distribution as shown in Fig. 21. In the multi-body dynamic model, a distributed aerodynamic pressure is exerted to the compliant skin outer surface to simulate the flight condition in drooped case defined in Section 1. As shown in Fig. 21, it can be seen that the maximum stress is about 626.6 MPa which is far less than the yield strength of Ti-6Al-4V. Finally, all linkages were milled by a numerical controlled machine toll, and the variable-thickness compliant skin and the four stringers were co-cured in an autoclave.

In order to demonstrate the feasibility of the morphing leading-edge concept, a drooping test was performed for the physical mockup. As a preliminary research and limited by budget, distributed aerodynamic forces were not exerted on the complaint skin in test but simulated by a multi-body dynamic analysis instead as shown in Fig. 21. The deference between the test without pressure and the simulation with pressure will be examined in the following. Fig. 22 shows that the measuring system for the compliant skin drooping test. The mock-up is assembled with a wing box providing fixed boundary condition and the actuating system is also embedded in the wing box. In the measuring system, an ARAMIS 3D Camera system is included which is a non-contact optical measuring

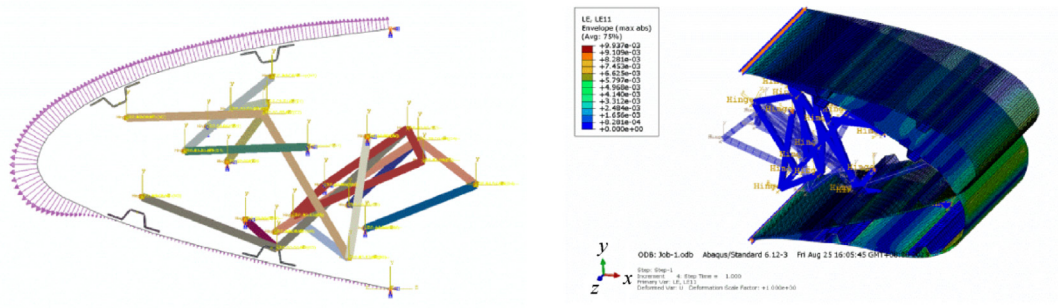

(a) Muti-body dynamic model of morphing leading-edge (b) Strain contour of muti-body dynamic analysis

**Fig. 19** Multi-body dynamic analysis of morphing leading-edge.

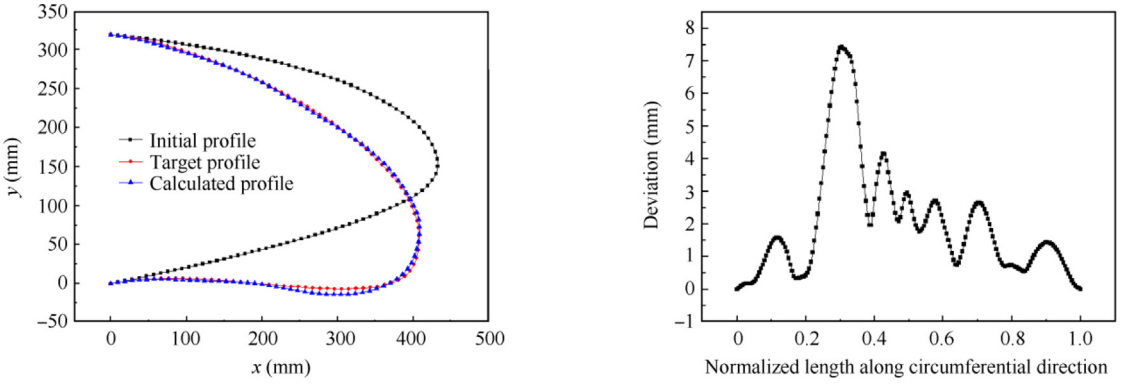


(a) Initial, target and calculated profile of morphing lead-ing-edge (b) Deviation distribution along circumferential direction

**Fig. 20** Comparison between target and calculated profile of morphing leading-edge.

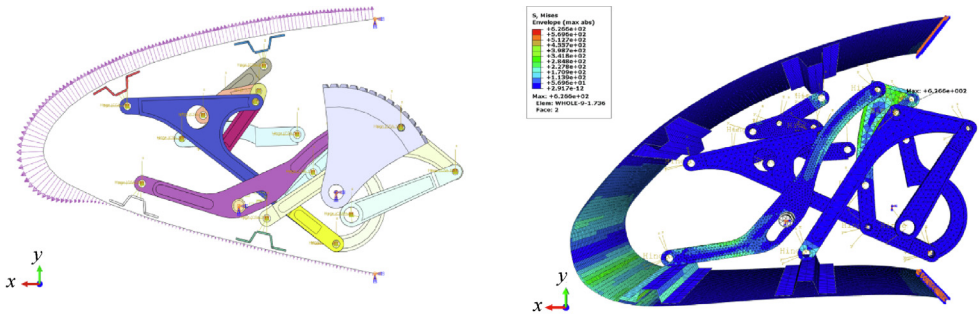

(a) Multi-body dynamic analysis model of morphing leading-edge mock-up before being driven

(b) Stress contour of morphing leading edge mock-up after being driven

**Fig. 21** Multi-body dynamic analysis of inner kinematic mechanism in drooped position with aero-loads.

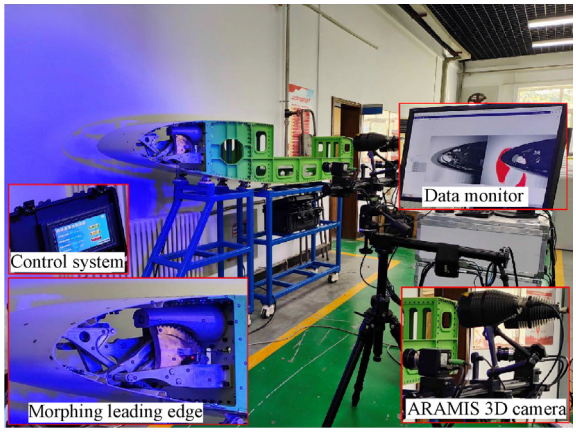


**Fig. 22** Measuring system for compliant skin drooping test.

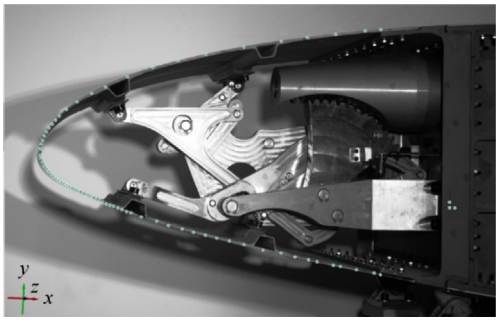

**Fig. 23** Mark points pasted on surface of lateral edge of compliant skin.

instrument based on a digital image correlation principle manufactured by GOM. The system can offer a high and stable solution for full-field and point-based analyses of test objects of a structural components of several meters in size. The ARAMIS 3D Camera system consists of two cameras placed at left and right position in front of the test object. The captured image data is processed by an image data analysis software and shown on the data monitor simultaneously. In addition, there is control system utilized to control the drooping process of the morphing leading-edge. As the measuring principle is based on the analysis of the point data of the captured images, some marked points should be pasted on the surface of the compliant skin lateral edge to establish a coordinate system. Fig. 23 shows the marked points pasted on the surface of the lateral edge of the compliant skin. More intense points are marked at the most leading end to improve the measure solution of points with large displacement.

Through the combination of the two images, the coordinates of the mark points can be calculated precisely. Fig. 24 shows the captured images of the left and right cameras before and after drooping. Fig. 25 presents the comparison of the profiles of the initial, target and tested results and Fig. 26 presents the deviation distribution of the test and simulation results. It can be seen that the tested initial profile in general agrees well with the theoretical initial profile with a maximum deviation of 3.87 mm located around the upper surface which means that manufacturing or measuring errors exist boxed as shown in Fig. 25. And the final drooped profile agrees well with the target profile in general. However, the maximum deviation is around 9.14 mm which is greater than the deviation value in the simulation phase and located at the most leading end. The relative deviation is around 2% defined by the ratio of the deviation to the chord length of the leading-edge. By further examining the deviation distribution in the Fig. 26, some interesting phenomenon can be found. Firstly, it can be seen that the maximum deviation value of the drooped case in test without pressure is almost the same with that in simulation with pressure as highlighted by an orange box. In consideration of the maximum deviation value after compliant skin design as shown in Fig. 12 and that after mechanism design as shown in Fig. 20, it is easy to a conclusion that the maximum deviation in test and final simulation is originated from the kinematic design error. Secondly, as highlighted by a green dash line box in Fig. 26, it can be seen that the manufacturing error in initial case as shown by black line is very large, and it is further transferred to the drooped case and produce a large deviation value as shown is red line. In addition, it also can be partly originated from the absence of the aerodynamic suction peak on the upper surface. All these deviation values can be decreased further through increasing the number of sets of the four-bar linkage system or performing a more elaborate design of the compliant skin and the mechanism. Despite the fact that the final deviation value is a little bit higher than expected, the drooped profiles in test and simulation maintain

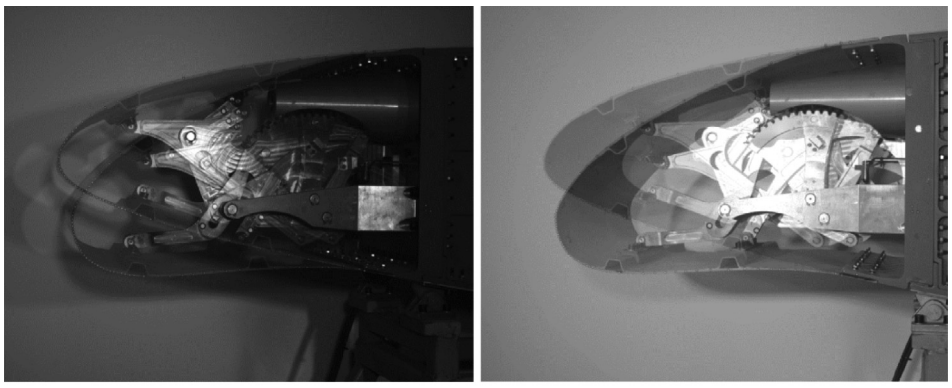

(a) Left camera image (b) Right camera image

**Fig. 24** Captured results of left and right camera for morphing leading-edge.

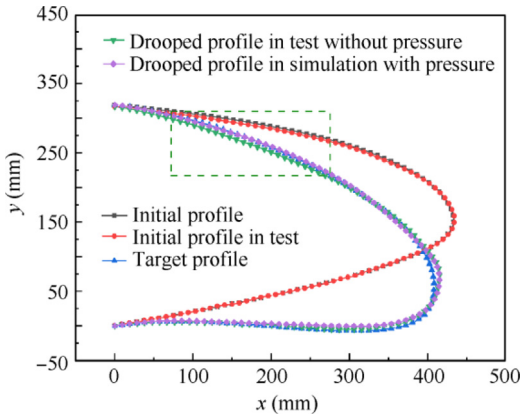


**Fig. 25** Initial, target and drooped profiles in different conditions.

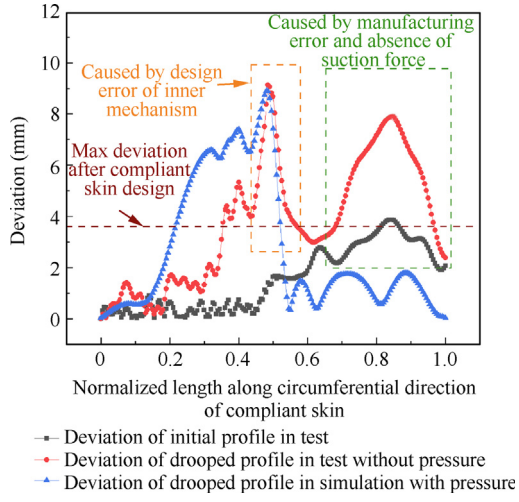


**Fig. 26** Comparison of deviation between different conditions.

a smooth and continuous curvature and it would not cause a severe inverse impact for the aerodynamic performance in drooped case. However, the specific impact will be further investigated in the future work through a CFD analysis or a wind tunnel test.

## 6. Conclusions

In summary, a two-step approach of morphing leading-edge design is developed and demonstrated. In the first step, a fiber continuity model based on the ply-drop sequence is proposed for the description of the variable-thickness compliant skin of a morphing leading-edge. Based on the model and a genetic algorithm, a collaborative optimization approach is established for the composite compliant skin design where several discrete and continuous variables exist. In the second step, an optimization approach of the inner closed-chain kinematic mechanism is proposed and a coupling method for the inner individual four-linkage systems is developed based on an inversion method. The final design and test results show that:

(1) The compliant skin can be drooped into the target profile with a maximum deviation of about 3.6 mm in simulation and 9.14 mm in real test.
(2) The optimized stacking sequences in different regions meets the ply continuity requirement and other manufacturing constraints of composite laminates well.
(3) the test results verify the effectiveness of the proposed optimization approach for variable-thickness compliant skin and the inner kinematic mechanism of the morphing leading-edge.

In order to enhance the applicability of the morphing leading-edge for real civil aircraft, some other aspects should be further taken into account. Actually, the weight and power balance is one of the crucial aspects of morphing leading-edge design, and a more detailed weight and power analysis should be considered and compared with a conventional one in the future. Moreover, to improve the airworthiness of the novel device, a fault and hazard analysis, control strategy design, and bird-impact resistance development are also needed to be examined further.

## CRediT authorship contribution statement

**Zhigang WANG:** Writing – original draft, Validation, Software, Methodology, Investigation, Conceptualization. **Xiasheng SUN:** Writing – review & editing, Supervision, Funding acquisition, Conceptualization. **Yu YANG:** Supervi-

sion, Funding acquisition, Formal analysis. **Wenjie GE:** Methodology, Data curation. **Daochun LI:** Writing – review & editing, Supervision, Funding acquisition. **Jinwu XIANG:** Supervision, Project administration. **Panpan BAO:** Visualization, Validation, Software. **Qi WU:** Visualization, Validation, Software, Conceptualization. **Andrea DA RONCH:** Writing – review & editing, Software.

## Declaration of competing interest

The authors declare that they have no known competing financial interests or personal relationships that could have appeared to influence the work reported in this paper.

## Acknowledgements

This work was supported by the National Research Project "Variable CAmber wing TechNology (VCAN)", China.

## References

1. Air Transport Action Group [Internet]. Geneva: Air Transport Action Group; [cited 2023 Oct 17]. Available from: https://aviationbenefits.org/environmental-efficiency/climate-action/waypoint-2050/.
2. International Civil Aviation Organization [Internet]. Montreal: International Civil Aviation Organization; [cited 2023 Oct 17]. Available from: https://www.icao.int/environmental-protection/Pages/envrep2022.aspx.
3. Bolonkin A, Gilyard G. Estimated benefits of variable-geometry wing camber control for transport aircraft. Washington, D.C.: National Technical Information Service (NTIS); 1999. Report No.: NASA/TM-1999-206586.
4. Reckzeh D. Multifunctional wing moveables: Design of the A350XWB and the way to future concepts. *29th congress of the international council of the aeronautical sciences*; St. Petersburg, Russia. 2014.
5. Strüber H. The aerodynamic design of the A350 XWB-900 high lift system. *29th congress of the international council of the aeronautical, sciences*; St. Petersburg, Russia. 2014.
6. Streett C, Casper J, Lockard D, et al. Aerodynamic noise reduction for high-lift devices on a swept wing model. *44th AIAA aerospace sciences meeting and exhibit*; Reno, Nevada. Reston: AIAA; 2006.
7. Dobrzynski W. Almost 40 years of airframe noise research: What did we achieve? *J Aircr* 2010;**47**(2):353–67.
8. Wölcken PC, Papadopoulos M. Smart intelligent aircraft structures (SARISTU). *Proceedings of the final project conference*. Cham: Springer International Publishing; 2016.
9. Concilio A, Dimino I, Pecora R. SARISTU: Adaptive Trailing Edge Device (ATED) design process review. *Chin J Aeronaut* 2021;**34**(7):187–210.
10. Dimino I, Moens F, Pecora R, et al. Morphing wing technologies within the Airgreen 2 project. *AIAA scitech 2022 forum*; San Diego, CA & Virtual. Reston: AIAA; 2022.
11. De Gaspari A, Cavalieri V, Fonzi N, et al. Final validation and performance assessment of a full-scale morphing droop nose demonstrator. *AIAA scitech 2023 forum*; National Harbor, MD & Online. Reston: AIAA; 2023.
12. Contell Asins C, Landersheim V, Wacker JD, et al. Design of a morphing leading edge as a high lift device for a regional aircraft. *IOP Conf Ser: Mater Sci Eng* 2021;**1024**(1):012033.
13. De Gaspari A, Gilardelli A, Ricci S, et al. Design of a leading edge morphing based on compliant structures in the framework of the $CS_2$-AIRGREEN2 project. *Proceedings of ASME 2018 conference on smart materials, adaptive structures and intelligent systems;* San Antonio, Texas, USA. New York: ASME; 2018.
14. Cavalieri V, De Gaspari A, Ricci S. Design and testing of a droop nose morphing for advanced regional aircraft: Numerical and experimental validation. *19th international forum on aeroelasticity and structural dynamics (IFASD 2022)*; Madrid, Spain. 2022.
15. Ameduri S, Amoroso F, Carossa GM, et al. An overview of the AG2 Project: Latest achievements. *AIAA scitech 2022 forum*; San Diego, CA & Virtual. Reston: AIAA; 2022.
16. Concilio A, Ameduri S, Dimino I, et al. An overview of adaptive structures engineering activities at CIRA. *AIAA scitech 2022 forum*; San Diego, CA & Virtual. Reston: AIAA; 2022.
17. Sofla AYN, Meguid SA, Tan KT, et al. Shape morphing of aircraft wing: Status and challenges. *Mater Des* 2010;**31**(3):1284–92.
18. Vasista S, Tong LY, Wong KC. Realization of morphing wings: A multidisciplinary challenge. *J Aircr* 2012;**49**(1):11–28.
19. Sun J, Guan QH, Liu YJ, et al. Morphing aircraft based on smart materials and structures: A state-of-the-art review. *J Intell Mater Syst Struct* 2016;**27**(17):2289–312.
20. Zhu LQ. Intelligent and flexible morphing wing technology: A review. *J Mech Eng* 2018;**54**(1):28.
21. Heo H, Ju J, Kim DM. Compliant cellular structures: Application to a passive morphing airfoil. *Compos Struct* 2013;**106**:560–9.
22. Ozel C, Ozbek E, Ekici S. A review on applications and effects of morphing wing technology on UAVs. *Int J Aviat Sci Technol* 2020;**1**(1):30–40.
23. Li DC, Zhao SW, Da Ronch A, et al. A review of modelling and analysis of morphing wings. *Prog Aerosp Sci* 2018;**100**:46–62.
24. Barbarino S, Bilgen O, Ajaj RM, et al. A review of morphing aircraft. *J Intell Mater Syst Struct* 2011;**22**(9):823–77.
25. Li YZ, Ge WJ, Zhou J, et al. Design and experiment of concentrated flexibility-based variable camber morphing wing. *Chin J Aeronaut* 2022;**35**(5):455–69.
26. Morishima R, Guo SJ, Ahmed S. A composite wing structure with a morphing leading edge. *51st AIAA/ASME/ASCE/AHS/ASC structures, structural dynamics, and materials conference*; Orlando, Florida. Reston: AIAA; 2010.
27. Monner H, Kintscher M, Lorkowski T, et al. Design of a smart droop nose as leading edge high lift system for transportation aircrafts. *50th AIAA/ASME/ASCE/AHS/ASC structures, structural dynamics, and materials conference;* California Reston: AAA: Palm Springs; 2009.
28. Kintscher M, Wiedemann M, Monner HP, et al. Design of a smart leading edge device for low speed wind tunnel tests in the European Project SADE. *Int J Struct Integr* 2011;**2**(4):383–405.
29. Rudenko A, Hannig A, Monner HP, et al. Extremely deformable morphing leading edge: Optimization, design and structural testing. *J Intell Mater Syst Struct* 2018;**29**(5):764–73.
30. Vasista S, Nolte F, Monner HP, et al. Three-dimensional design of a large-displacement morphing wing droop nose device. *J Intell Mater Syst Struct* 2018;**29**(16):3222–41.
31. Radespiel R, Heinze W. SFB 880: Fundamentals of high lift for future commercial aircraft. *CEAS Aeronaut J* 2014;**5**(3):239–51.
32. Contell Asins C, Landersheim V, Laveuve D, et al. Analysis and design of a leading edge with morphing capabilities for the wing of a regional aircraft—gapless chord- and camber-increase for high-lift performance. *Appl Sci* 2021;**11**(6):2752.
33. Wang C, Haddad Khodaparast H, Friswell MI, et al. Conceptual-level evaluation of a variable stiffness skin for a morphing wing leading edge. *Proc Inst Mech Eng Part G J Aerosp Eng* 2019;**233**(15):5703–16.
34. Fortin F. Shape optimization of a stretchable drooping leading edge. *AIAA scitech 2019 forum*; San Diego, California. Reston: AIAA; 2019.
35. Zhang YQ, Ge WJ, Zhang ZA, et al. Design of compliant mechanism-based variable camber morphing wing with nonlinear large deformation. *Int J Adv Rob Syst* 2019;**16**(6):172988141988674.

36. Vasista S, De Gaspari A, Ricci S, et al. Compliant structures-based wing and wingtip morphing devices. *Aircraft Eng & Aerospace Tech* 2016;**88**(2):311–30.
37. Sodja J, Martinez MJ, Simpson JC, et al. Experimental evaluation of the morphing leading edge concept. *23rd AIAA/AHS adaptive structures conference;* Kissimmee, Florida. Reston: AIAA; 2015.
38. Wang ZG, Yang Y. Design of a variable-stiffness compliant skin for a morphing leading edge. *Appl Sci* 2021;**11**(7):3165.
39. Yang Y, Wang ZG, Wang BW, et al. Optimization, design and testing for morphing leading edge. *Proc Inst Mech Eng Part C J Mech Eng Sci* 2023;**237**(18):4100–11.
40. Yang Y, Wang ZG, Lyu SS. Comparative study of two lay-up sequence dispositions for flexible skin design of morphing leading edge. *Chin J Aeronaut* 2021;**34**(7):271–8.
41. Gebbink R, Wang GL, Zhong M. High-speed wind tunnel test of the CAE-AVM in DNW-HST for CFD validation purposes. *Proceedings of the 55th AIAA aerospace sciences meeting*; Grapevine, Texas. Reston: AIAA; 2017.
42. Hua J, Zhong M, Zheng S, et al. Design and database applications of CAE-AVM model cruise configuration. *Acta Aerodynamica Sinica* 2022;**40**(4):133–47,132 [Chinese].
43. Zhong M, Hua J, Wang H, et al. Design and verification of high-lift configuration of civil aircraft standard model CAE-AVM-HL. *Acta Aerodynamica Sinica* 2022;**40**(4):158–67 [Chinese].
44. Tsai SW. Composites design. Dayton: Think Composites; 1987.
45. Thuwis GA, Abdalla MM, Gürdal Z. Optimization of a variable-stiffness skin for morphing high-lift devices. *Smart Mater Struct* 2010;**19**(12):124010.
46. De Gaspari A, Riccobene L, Ricci S. Design, manufacturing and wind tunnel validation of a morphing compliant wing. *J Aircr* 2018;**55**(6):2313–26.
47. McCarthy JM, Soh GS. Geometric design of linkages. Berlin: Springer Science & Business Media; 2010.
48. Daniel K, Roland S. Dynamic mechanism design. *An introduction to the theory of mechanism design*. New York: Oxford University Press; 2015. p. 204–34.